PROCEEDINGS OF SPIE

SPIEDigitalLibrary.org/conference-proceedings-of-spie

Low-cost cryogenic technologies for high-operating temperature infrared imaging

A. Veprik, D. Gedeon, R. Radebaugh, R. Refaeli, S. Kurucz, et al.

A. Veprik, D. Gedeon, R. Radebaugh, R. Refaeli, S. Kurucz, L. Bunin, "Low-cost cryogenic technologies for high-operating temperature infrared imaging," Proc. SPIE 12534, Infrared Technology and Applications XLIX, 125340C (13 June 2023); doi: 10.1117/12.2664389

SPIE.

Event: SPIE Defense + Commercial Sensing, 2023, Orlando, Florida, United States

Low-cost cryogenic technologies for high operating temperature infrared imaging

A Veprik[†], D Gedeon[††], R Radebaugh[†††], R Refaeli[†], S Kurucz[†] and L Bunin[†]

[†]CRYOTECH LTD, Ein Harod Meuhad, 1896500, Israel
[††]GEDEON ASSOCIATES, 16922 South Canaan Rd, Athens, OH 45701, USA
[†††] RADEBAUGH CRYOGENICS, 335 Gorham Ct. Louisville, CO 80027, USA

ABSTRACT

Technological innovations advance the state of the art for low size, weight, and power (SWAP) cryocoolers for high operating temperature infrared imaging. The authors present essentials of mechanical design, outcomes of theoretical modeling/optimization and initial testing for a cost-effective low SWAP split Stirling crycooler.

Keywords: low cost, low SWaP, integration, HOT infrared imaging

1. INTRODUCTION

Most of the commercially available low size, weight, and power (SWAP) cryocoolers for high operating temperature (HOT) infrared (IR) imaging are just downscaled replicas of the low-temperature predecessors. Unfortunately, their further down-scaling and cost reduction potential is already exhausted, thus the further progress will not be possible without development and deployment of novel and low-cost cryogenic technologies.

From the very moment of its inception in 2018, CryoTech has focused on disruptive innovation enabling drastic lowering of ownership costs by deploying alternative commercially off the shelf available technological solutions and components. The list of novelties enabling further improvement of SWAP and cost indices includes but is not limited to using an alternative low leaking working agent, nylon microfiber "parallel wire" regenerator, an inverted "moving magnet" actuator featuring a built-in nonlinear magnet spring, a resonant rodless pneumatic displacer assisted by a magnet spring, simplified cold finger, etc.

These technologies have successfully passed the experimental feasibility phase and are implemented in the design of a cost-effective low SWAP split Stirling crycooler [1-3]. In this paper, the authors report on the project status and discuss the theoretical basis for these innovations.

2. ALTERNATIVE WORKING FLUID

Typical tactical Stirling cryocoolers as used for maintaining IR focal plane arrays at cryogenic temperatures usually operate using gaseous helium. This working fluid features the favorable and unique combination of low saturation temperature, low viscosity, high thermal conductivity, high heat capacity and behaves essentially like an ideal gas over the entire range of temperatures and charge pressures.

The disadvantages of using helium are many. To start with, because of the small size of molecules, helium is prone to fast leakage out of sealed pressure vessels through inevitable serpentine leak channels formed by nano-scaled defects. Long-term sealing of pressurized helium is, therefore, something of a black art and requires using special low permeable alloys, helium-tight feedthroughs (in case of internal placement of driving coils) along with crushed metal seals. Another issue may be attributed to a high rate of diffusivity of water vapor (major pollutant) into helium [4]. Loss of working agent and internal contaminations are the primary failure mechanisms limiting the life of linear cryogenic coolers [5].

The authors recently realized that the use of helium for HOT Stirling cryocoolers operating at temperatures well in excess of 77K is not mandatory anymore. Replacement of helium by an alternative working fluid having larger molecules may

Infrared Technology and Applications XLIX, edited by Gabor F. Fulop, David Z. Ting,
Lucy L. Zheng, Proc. of SPIE Vol. 12534, 125340C · © 2023 SPIE
0277-786X · doi: 10.1117/12.2664389

substantially eliminate the loss of the working fluid in the first place. Further, the gaseous working fluid for Stirling cryocoolers may be engineered/chosen so as to take advantage of the real-gas interaction between molecules during expansion processes near the vapor-liquid saturation temperature. This effect is dominant in vapor-compression or Joule-Thomson refrigeration cycles, where the working fluid is alternately condensed to liquid under high pressure, moved to a different location, then vaporized under low pressure, rejecting then accepting large amounts of heat (latent heat of vaporization) for little temperature change. In the case of a Stirling cryocooler this effect can increase the cooling power by reducing the net enthalpy transport loss in the regenerator.

The property of interest is the change of mass-specific enthalpy, h, with pressure, P, which can be expressed in the form $(\partial h/\partial P)_T = v(1-\beta T)$, where v is specific volume, T is absolute temperature and β is the volumetric coefficient of expansion $\beta = v^{-1}(\partial v/\partial T)_p$. This property gives rise to a pressure-dependent component of enthalpy flow in the regenerator superimposed on the temperature-dependent component typical of an ideal gas. The pressure-dependent enthalpy can flow in either direction, depending on whether $\beta T > 1$ or $\beta T < 1$. For the case $T\beta > 1$ it flows toward the warm end of the regenerator, boosting cooling power, under the typical phasing between pressure fluctuation and fluid mass flow rate. For the case $\beta T < 1$, the pressure-dependent enthalpy flows toward the cold end, which is to be avoided. The secondary cooling effect may be thought of as positive localized Joule-Thomson cooling resulting from the work done by the compressed working fluid against forces of intermolecular attraction while increasing the distances between molecules. Indeed, the Joule-Thomson coefficient $\mu_{JT} = C_P^{-1}(\beta T - 1)v$, where C_P is the isobaric specific heat, will be positive for $\beta T > 1$.

For example, nitrogen may be thought of as a suitable working fluid. With a saturation temperature around 110K at a typical charge pressure of 1.2 MPa its βT value is well in excess of unity over the temperature range 120-200K, flattening asymptotically to unity at typical ambient temperatures, as shown in Figure 1. Figure 2 shows the example of simulated reduction of power consumed by the same cryocooler (acceptor temperature 150K, reject temperature 300K) charged by nitrogen and helium at different added heat loads. The simulations were performed for CryoTech split Stirling cryocooler, as described in [1-3], using Sage Low-T cooler software [6] which supports real-gas equation of state and transport properties derived from NIST REFPROP fluid properties [7]. It is worth noting that in both cases, for each working point we optimized the geometry of regenerator, charge pressure, driving frequency and spring rate of the displacer spring. From Figure 2, nitrogen outperforms helium over the entire range of added heat loads, especially at low powers. It is worth noting that typical working range of added heat load for this class of cryocoolers is 50-100mW.

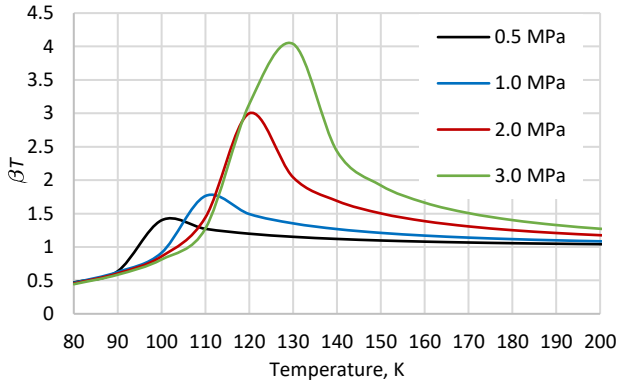

Figure 1. βT vs T for nitrogen at different charge pressures

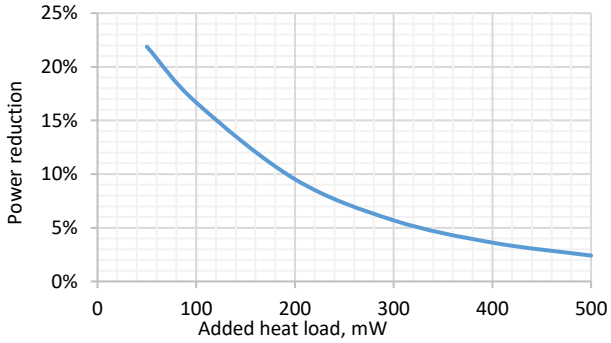

Figure 2. Sage simulated power reduction using nitrogen compared to helium

Appreciation and study of βT effects in regenerators of Stirling cryocoolers is not new. It has been a topic of interest for many years for helium-charged cryocoolers operating near 4 K [8]. To our knowledge the present paper is the first to explore the enhancement for nitrogen-charged Stirling cryocoolers at higher temperatures.

Regarding other gas properties, nitrogen has similar viscosity to helium, but much lower thermal conductivity. Specifically, in small tactical cryocoolers the geometry of the cold finger and, therefore, regenerator are usually specified prior to a development of the cryocooler and are dictated by the existing standards, ability to withstand adverse shock and vibration environment conditions, available manufacturing technologies, geometry of the commercially available components of the vacuum package (e.g. Dewar shroud, feedthrough), etc.

Therefore, in small, low-power, tactical cryocoolers the regenerators are usually oversized and low thermal conductivity of working fluid is not a problem because surface-to-volume ratios are so high that heat transfer is generally not an issue. It is worth noting that small heat conductivity of nitrogen reduces the gas related component of the parasitic axial heat conductance.

3. NYLON PARALLEL WIRE REGENERATOR

The regenerator is the key component of a cryogenic cooler, having a significant influence on the overall performance. The regenerators of tactical Stirling cryocoolers are typically engineered in the form of thousands of metallic woven mesh disks, which are then stacked inside the bore of a tubular displacer cartridge. With high wetted-surface-to-volume ratios such stacked-mesh regenerators are very effective but have inherently low ratios of heat transfer to pressure drop (compared to parallel flow geometries). At a microscopic level the working fluid flows across wires in a zig-zag fashion with abrupt expansions and contractions resulting in tiny wakes and eddies similar to the velocity fluctuations of turbulent flow. This produces an effective diffusivity of heat and momentum in the working fluid much higher than the molecular diffusivity. In other words, the flow irregularities increase the effective conductivity and viscosity of the working fluid.
Another disadvantage of such a regenerator is the inherently high axial anisotropy of the regenerator matrix primarily attributed to the manufacturing technique. Highly porosity regenerators may be prone to axial migration of regenerator screens under high acceleration forces, resulting in local compacting/inclining of mesh disks eventuating in a build-up of void volumes. Specifically, displacers from the same batch may be quite disparate in terms of heat exchange performance. Also, the raw material (SST wire mesh, typically) is quite expensive, the waste rate is high, the entire manufacturing procedure is quite laborious and requires special equipment and skills. Further, from simulations, high temperature and high-frequency cryocoolers operate best with highly porous regenerators in excess of 85% and with wire diameters below 10um. Unfortunately, the finest commercially available stainless-steel screens (e.g. #635) have a minimum wire diameter of 20 um. Moreover, technological constraints do not allow making reasonably priced regenerators with porosities higher than 70%. Finally, the weight added by a metallic regenerator increases the vibration export and requires higher driving force, thus increasing power consumption.
Among other alternative topologies, we considered "parallel wire" regenerator in the form of a bundle of straight fibers aligned along the length of displacer tube, as detailed in [9], the authors of which experimented with stainless steel parallel wire regenerators and demonstrated that they may have sufficient heat exchange performance at exceptionally low flow friction. In particular, they experimentally evaluated dependence of the Fanning friction factor on the Reynolds number, Re, in the form $f_F \approx 14.7/Re$. It is worth noting that for the laminar flow in circular unobstructed tubes $f_F \approx 16/Re$. Obvious disadvantage of such a regenerator made of stainless-steel wires is the gross parasitic axial heat conduction produced by a continuous metallic conduction paths along the regenerator. Additionally, the manufacturing technique detailed in [9] is quite laborious and expensive.
We describe here the development of a parallel fiber regenerator made of commercially off the shelf available material in the form of a round (∅5mm) cartridge containing a bundle of nylon fibers wrapped in a foil made of the same material, which has significantly reduced parasitic axial conduction as compared with a stainless steel parallel wire regenerator.
In particular, from experimentation [1-3], the best performance was achieved with nylon fibers having diameter $d_w = 9.5\ um$ and porosity 79%. Figure 3 shows this material (left) and displacer tube (right) to which the regenerator cartridge may be simply press-fit inserted in no time. It is important to notice that prior to the cryocooler assembly each displacer has to be dried for 10 minutes using a flow of warm dry nitrogen.

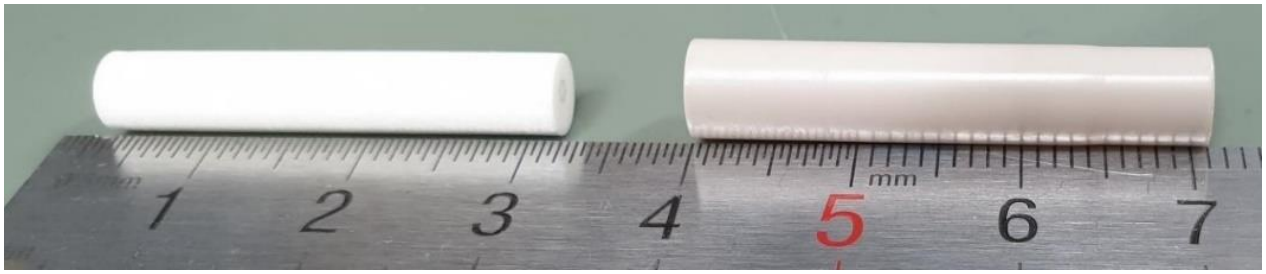

Figure 3. Commercially of the shelf available regenerator material and displacer tube prior to assembly

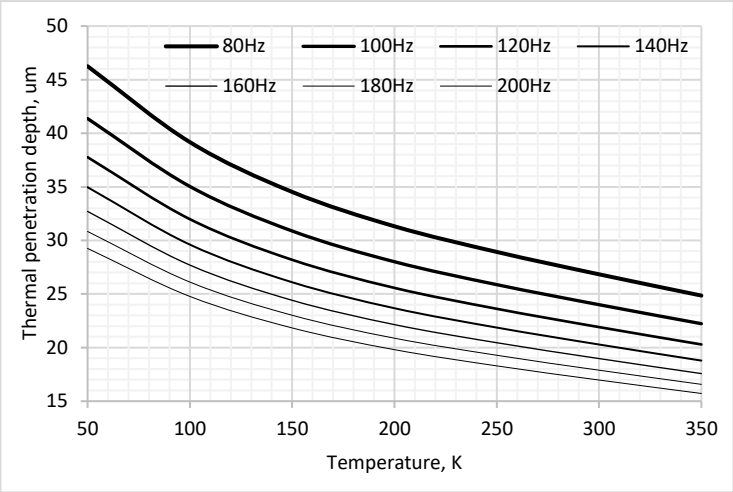

Figure 4. Thermal penetration depth of nylon at different temperatures and working frequencies

Thermal penetration depth

To start with, it was important to make sure that the heat penetration depth δ_t of the chosen material is larger than the half of diameter of the fibers $\delta_t \geq d_w/2 = 4.75um$, thus enabling full use of the regenerator material. Figure 4 shows the dependence of the thermal penetration depth for oscillating heat transfer on the temperature, at different driving frequencies. The evaluations were performed using temperature dependent specific heat $C_P(T)$, heat conductivity, $k(T)$, and density, ρ, of the regenerator material equation using expression $\delta_t = \sqrt{\frac{k}{\pi \rho C_p f}}$. From Figure 4, over the typical temperature range 50K to 350K and frequency range 80Hz to 200Hz, the chosen material enables the full use of the material.

Fanning friction factor

Further, we evaluated the dependence of the Fanning friction factor on the Reynolds number. The experimentation was performed using the test station comprising dynamic pressure regulator and flow meter as shown in Figure 5.

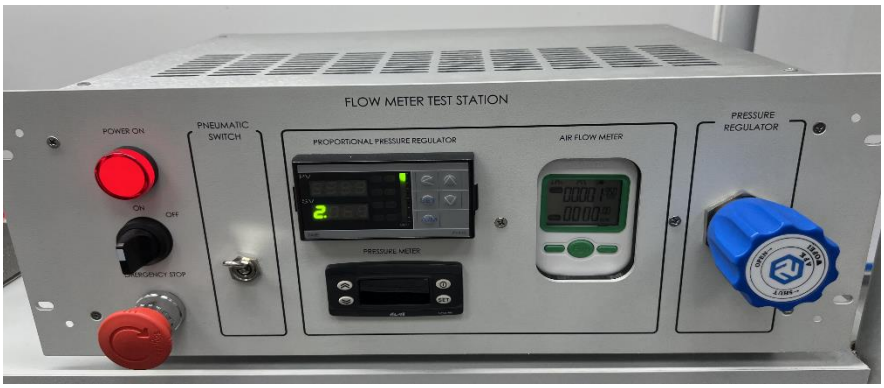

Figure 5. Test station

Figure 6.a shows the experimentally evaluated dependence of the flow rate on the pressure drop at the exit pressure 1 bar. The incremental pressure drop along the length of the regenerator may be expressed using Fanning friction factor, f_f, mass flow rate, $\dot{m}$, gas free flow area A_g and hydraulic diameter d_h in the form $dP = \frac{2 f_f (\dot{m}/A_g)^2}{\rho d_h} dx$.

Because the total pressure drop across the regenerator is not small compared with the exit pressure, the density varies considerably from one end to the other. We then make an ideal gas approximation and use the integral

$$\int_{P_1}^{P_2} PdP = (P_2^2 - P_1^2)/2 = \frac{2RTf_f(\dot{m}/A_g)^2 L}{d_h} \quad (1)$$

to find the Fanning friction factor, where R is the gas constant, $P_1 = 1\,bar$ and $P_2 = P_1 + \Delta P$. In addition, the hydraulic diameter may be expressed through the wire diameter d_w and porosity η in the form $d_h = \frac{\eta d_w}{1-\eta}$. The Reynolds number

was calculated using $Re = \frac{\dot{m} d_h}{A_g \mu}$, where μ is the fluid viscosity. In Figure 6.b, the solid bold line presents calculated dependence of the Fanning friction factor evaluated using (1) on the Reynolds number; it may be accurately approximated by the power function in the form $f_F = 7.15 Re^{-0.846}$. For the reference, lines are superimposed representing dependences of the Fanning friction factor of the unobstructed laminar flow in the circular tubes, $f_F = 16 Re^{-1}$, and this for the stacked screens, $f_F = 129 Re^{-1} + 2.921 Re^{-0.103}$ [6]. From Figure 6.b, such a regenerator indeed has exceptionally low friction factor.

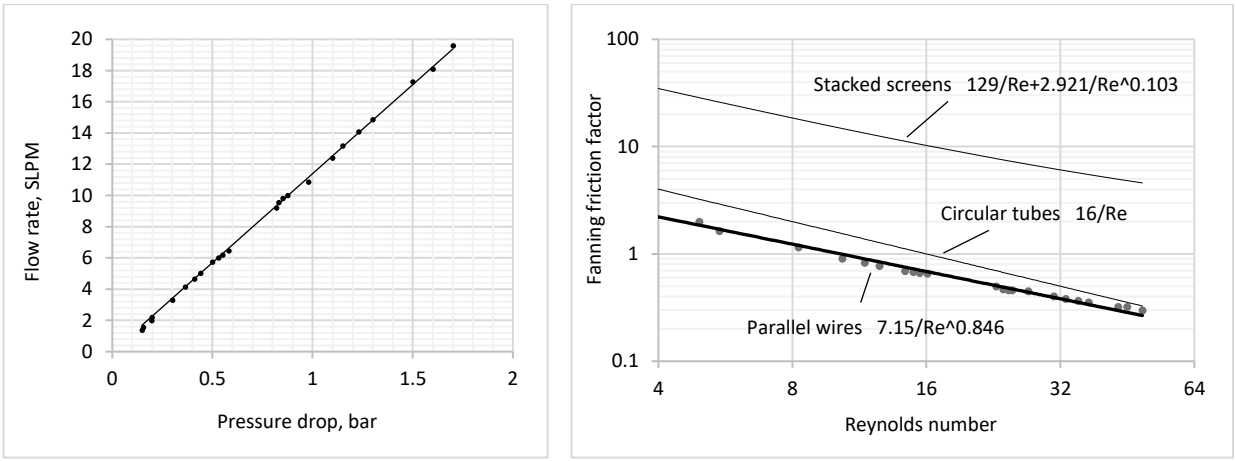

(a) (b)

Figure 6. Flow rate as a function of pressure drop (a) and Fanning friction factor as a function of Reynolds number (b)

Parasitic axial heat conductance

Axial heat conductance of the porous regenerator matrix may be evaluated using equation

$$\dot{Q} = f_c \frac{\pi D^2 (1-\eta)}{4L} \bar{K} \tag{2}$$

where D and L are diameter and length of the regenerator cartridge, respectively, T_h and T_c are the hot and cold temperatures of the regenerator matrix, $\bar{K} = \int_{T_c}^{T_h} k(T)\,dT$ - averaged heat conductivity of regenerator solid calculated using the temperature dependent thermal conductivity of the regenerator solid, $k(T)$. In equation (2), the conductivity degradation factor $f_c = 1$ for the parallel wire and $f_c = 0.13$ for the stacked screens geometries, respectively [10,11].

For the typical numerical values $D = 0.005m$; $L = 0.028m$; $T_h = 300K$; $T_c = 150K$, the parasitic axial heat conductance of parallel wire nylon regenerators with $\eta = 0.79$ and averaged heat conductivity $\bar{K} = 0.34\ Wm^{-1}K^{-1}$ is as low as 7.5 mW. For the reference, the axial heat conductance of stainless steel stacked screen regenerators having $\eta = 0.7$ and averaged heat conductivity $\bar{K} = 18.5\ Wm^{-1}K^{-1}$ is 76mW; this is ten-fold higher as compared to a nylon parallel wire regenerator. For the reference, the total heat load of the typical IDDA under such conditions is 120mW.

Hydraulic diameter

To ensure full participation of the working fluid in the heat exchange, the fluid thermal penetration depth δ_t must be comparable to or greater than the hydraulic diameter d_h. A reasonable requirement is $\delta_t \geq d_h/2$. For the specific regenerator material having $d_w = 9.5um$ and $\eta = 0.79$, the hydraulic diameter is $d_h = 36\ um$. Figure 7 shows dependence of the thermal penetration depth of nitrogen on the temperature at different driving frequencies. From Figure 7, nitrogen has a thermal penetration depth substantially larger than half of the hydraulic diameter over the entire range of temperatures and driving frequencies. The thermal penetration depth of Figure 7 applies to strictly laminar flow. In reality,

the presence of microscopic flow fluctuations in the actual regenerator matrix comprised of slightly curled fibers will increase the effective thermal penetration depth beyond the laminar value.

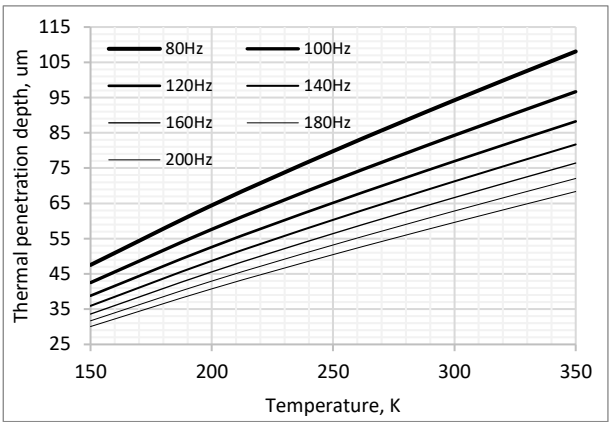

Figure 7. Thermal penetration depth of the working fluid.

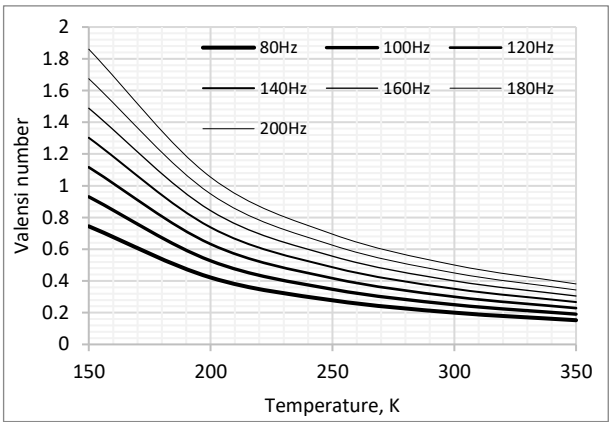

Figure 8. Valensi number of the working fluid.

Viscous penetration depth

The viscous penetration depth is given by

$$\delta_v(P,T) = \sqrt{\mu(P,T)/\pi f \rho(P,T)} = \sqrt{N_{\mathrm{Pr}}(P,T)}\,\delta_t(P,T) \tag{3}$$

where dynamic viscosity $\mu(P,T)$, Prandtl number $N_{\mathrm{Pr}}(P,T)$ and thermal penetration depth $\delta_t(P,T)$ in fluid are temperature and pressure dependent. In equation (3), $\delta_v(P,T)$ is comparable to $\delta_t(P,T)$ since $N_{\mathrm{Pr}}(P,T)$ is close to one for an ideal gas. The significance of $\delta_v(P,T)$ is not so well understood, but it is related to the Valensi number by $Va(P,T) = \left[d_h/\delta_v(P,T)\right]^2$. In order to use steady-state flow correlations in oscillation flow $Va(P,T)$ should be less than about 10. This requirement should be satisfied here at least for frequencies less than about 200 Hz, as shown in Figure 8 portraying dependencies of $Va(P,T)$ on the temperature at different driving frequencies. A low Valensi number indicates momentum has time to diffuse from one side of the channel to the other during a cycle.

Transverse diffusivity

Parallel channel regenerators excelling in all the above properties have been made in the past, often in the form of wrapped foils, uniformly spaced to produce uniform flow channels similar to parallel plates. These have typically failed to perform as expected because perfect spacing uniformity is difficult to achieve with the flexible foils used and small gaps required, leading to unequal flows in different parts of the regenerator. These unequal flows tend to produce non-uniform transverse temperature distributions and macroscopic flow circulations that degrade performance. To counter this, experience shows that some degree of transverse mixing of the regenerator flow (in planes perpendicular to the flow direction) is beneficial. For commercial polymeric fiber bundles, the fibers are curly and not perfectly packed together. Instead, there are random gaps between fibers that produce a network of non-uniform inter-connected flow channels. These produce microscopic flow fluctuations with effective enhancements of transport properties similar to stacked-mesh regenerators but not as extreme because the local flow-path expansions and contractions between mostly parallel fibers are much less than those of a stacked mesh. The result seems to be sufficient transverse mixing to stabilize the regenerator and prevent macroscopic flow circulations without unduly increasing flow resistance or longitudinal thermal diffusivity.

Thermal mass

Cooldown time or "time to image" is one of the major figures of merit characterizing modern IR imagers. It obviously depends on the gross cooling capacity of the associated cryocooler, values of cold and reject temperatures, parasitic conductive and radiative heat inflows and thermal mass of fully or partially cooled components of IDDCA. The fully cooled components are cold shield, cold filter, substrate, focal plane array and read-out-integrated circuit (ROIC). Partially cooled components are cold finger, displacer tube and regenerator matrix.

In the first approximation, the regenerator may be thought of as a circular porous rod having length L, diameter D and apparent density $(1-\eta)\rho$, where ρ is the density of solid material and η is the regenerator porosity. The specific heat $C(T)$ of the solid is temperature dependent. In the initial condition, the regenerator material has uniform temperature distribution $T(x) = T_{amb}$, where $x \in [0, L]$ is a distance from the warm end, T_{amb} is the ambient temperature. The operation of cryocooler results in transient cooling the cold end to T_c and transient heating the warm end of the regenerator to $T_r > T_{amb}$. It is worth noting that because of the typically fast cooldown times (less than 2 minutes) and relatively high thermal inertia of the mechanical components of the cold finger base and associated heatsink, $T_r \approx T_{amb}$. In the first approximation, therefore, the final temperature distribution at the end of cooldown time, may be thought of in the linear form $T(x) = T_{amb} - \frac{T_{amb} - T_c}{L} x$. In these notations, the thermal mass of regenerator during the transient cooling process may be assessed as

$$\mathbf{M} = (1-\eta)\rho \frac{\pi D^2}{4} \int_0^L \bar{C}\left[T_{amb}, T(x)\right]\left[T_{amb} - T(x)\right] dx \tag{4}$$

where $\bar{C}\left[T_{amb}, T(x)\right] = \frac{1}{T_{amb} - T(x)} \int_{T(x)}^{T_{amb}} C(T)\, dT$ is the averaged specific heat of the regenerator material at location x.

Over the typical temperature range 150K to 300K, the specific heats of SST304 and nylon may be linearly approached as $C_{SST}(T) = 1.075 \times T + 162.5$ and $C_{NYLON}(T) = 4.298 \times T + 341.7$, respectively, [12]. In case of linear dependence of heat capacity on temperature, $\bar{C}\left[T_{amb}, T(x)\right] = \frac{C\left[T_{amb}\right] - C\left[T(x)\right]}{2}$. Numerical calculations using (4) for parallel wire nylon $\left(\rho = 1150 kg/m^3;\ \eta = 0.79\right)$ and stacked screens stainless steel $\left(\rho = 8000 kg/m^3,\ \eta = 0.7\right)$ regenerators having the same diameter $D = 0.005m$, length $L = 0.028m$ and the same temperature distribution with $T_{amb} = 300K;\ T_c = 150K$ show that thermal masses are 14J and 43J, respectively. Recalling that the typical thermal mass of tactical HOT IDDA undergoing cooling from 300K to 150K is 120J, using the regenerator having by 29J smaller thermal mass may contribute to essentially faster cooldown times.

Optimum regenerator

Choosing regenerator geometry/material requires complex consideration of large numbers of, usually contradicting, factors. For example, the requirement of minimum void volume contradicts with requirement of low pressure drop and low axial heat conductance, the requirement of high heat conductance of the regenerator filaments contradicts with the requirement of low axial heat conductance, the requirement of high heat capacity contradicts with the requirement of fast cooldown and substantial thermal penetration depth. Parasitic axial thermal conductivity of the cold finger cannot be decreased by increasing the length and decreasing diameter without considering loss of dynamic stability under adverse environmental conditions along with dimensional constraints imposed by the design of an IR imager.

It is worth noting that, in practice, the geometry of the cold finger and its materials are usually specified prior to a development of the cryocooler and are dictated by the geometry of the commercially available components of the vacuum package like Dewar shroud, feedthrough, etc. Further, the cost-effective design of a cryogenic cooler may rely on using commercially available materials only. Therefore, not all the theoretically optimal materials/geometries are feasible and deployable.

The general approach adopted by CryoTech is that the design of low cost cryocooler should be governed by the choice of the suitable and commercially available low-cost regenerator material based on experimentation and evaluation of their physical properties.

There is a need to account for a joint dynamics of electromechanically driven compressor and pneumatically driven expander, especially in the case of a plungerless displacer which is driven by the drag force produced by the flow of the working agent along the porous material of regenerative heat exchanger. This is possible to do using full theoretical model of cryocooler, under Sage software.

The above-mentioned parallel wire regenerator with 9.5um nylon filaments and 79% porosity favorably combines suitable hydraulic diameter, thermal penetration depth, low axial heat conductance. Additionally, this material is in a wide use, costs only 10¢ per piece and may be easily press-fit integrated in no time into the confining displacer tube (see Figure 3).

Further, from experimentation with CryoTech cryocooler [1-3], such a material is suitable for plungerless displacers and shows excellent performance.

Based on the above experimentation, the Sage model of parallel-wire regenerator was updated, as shown in Figure 9. A sensitivity study varied the nylon wire diameter over the range 7 to 12um and found the optimum porosity at different added heat loads from 100 to 500mW.

The model employed Sage's generic matrix component for the parallel-wire regenerator. This component implements custom inputs for coefficients and exponents of standard correlating expressions for friction factor and Nusselt number. The coefficients for friction factor were set to experimentally derived values, presumed to apply over the entire range of study. There were no experimentally derived coefficients for Nusselt number on hand, so instead the model used an approximate value, as follows. Assuming the Reynolds number is low and the gas thermal penetration depth is large compared to the hydraulic diameter, the flow can be considered laminar with negligible entry length for developing flow. For that case Kays and London tabulated analytic solutions for simple geometries including an equilateral triangle duct, which is a reasonable approximation to the spaces between hexagonal close-packed fibers [13]. For that case the Nusselt number (under constant heat-flux boundary conditions) is simply a constant N_u = 3.11, without dependence on the Reynolds number.

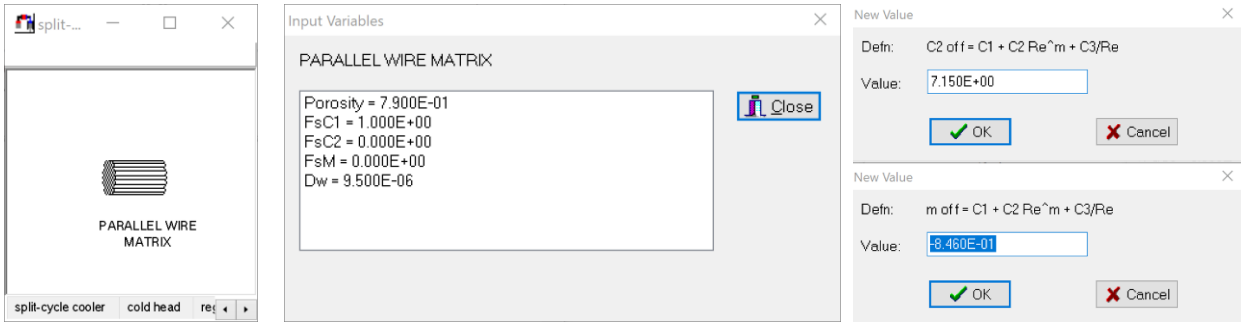

Figure 9 . Modelling parallel wire regenerator

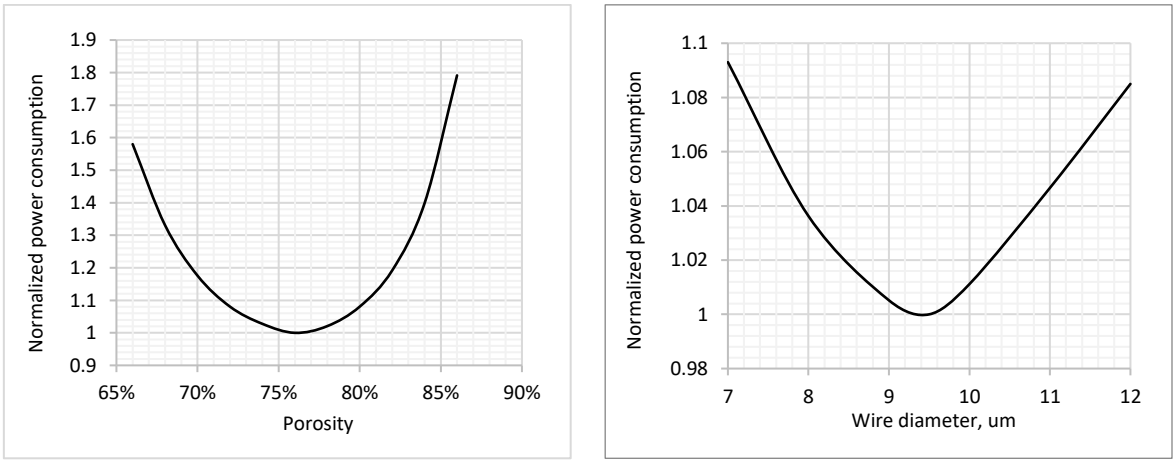

(a) (b)

Figure 10. Power consumption at different porosities (a) and wire diameters (b)

Figure 10 shows simulated dependencies of the normalized power consumption at a fixed wire diameter 9.5um on regenerator porosity (a) and on the wire diameter at a fixed porosity 79% (b). In Figure 10, the power consumption is normalized by the power consumption at the optimal wire diameter and porosity, 9.4um and 76%. From Figure 10, the material of choice may be considered as optimal for the purpose. Available hydraulic diameters are in an ideal range for regenerators to provide good heat transfer and low pressure drop. The ease of integration into a confining displacer tube leads to the low incurred cost.

4. PLUNGERLESS DISPLACER WITH MAGNET SPRING

Traditionally, a spring-assisted resonant displacer of a split Stirling cryocooler is actuated by a small differential piston which is disposed coaxially and slidably inside a tightly matched differential cylinder, thus forming two collinear close clearance seals bounding the so-called "warm chamber", which is connected by a duct to the compression chamber of an associated piston compressor. These clearance seals must be individually matched by machining to a micrometer accuracy of hard and wear-resistant materials like hardened high-speed steel or ceramics. The tail of the differential piston is protruding into the sealed rear chamber, thus forming the pneumatic spring. It is worth noting that pneumatic spring is not capable of axial centering the displacer assembly and preventing from axial drifting, thus the rear chamber usually houses an auxiliary mechanical spring. Such an arrangement adds mechanical complexity, bulk to the rear side of the cold head, and weight to the moving assembly.

Additionally, the concept of plunger-driven actuation, as explained above, requires the use of highly accurate and quite expensive cold fingers. Specifically, the bores of the cold finger tube and cold finger base which are used for nesting the above-mentioned differential cylinder have to be precisely aligned and concentric within a typical 30um tolerance. Such an accuracy is usually achieved by a quite expensive machining of the entire cold finger of a single workpiece of low heat conductive material, such as titanium alloy Ti 6Al-4V ELI (grade 23). It is worth noting that the relatively low module of elasticity E=96 GPa and constraints imposed on the dynamic response of IR focal plane array (FPA) under adverse environmental conditions prevent thinning the cold finger tube below a particular 100um limit, typically. In some events, there is a need for adding a low heat-conductive front support of the cold finger tip resulting in mechanical complexity and additional parasitic conductive heat inflow. Another disadvantage is related to the low heat conductivity of the titanium cold finger; this complicates the heat rejection and affects the performance of the cryocooler. Also, since titanium alloys cannot be welded/brazed directly to other metals, there is a need for at least two hybrid rings for welding the cold finger plug (Invar, typically) and the shroud of the evacuated Dewar (Kovar, typically). Such hybrid rings are usually made by explosion welding and, therefore, are extremely expensive. Also, high-temperature brazing of titanium alloys may lead to unfavorable thermal strains, phase transitions, embrittlement, and micro-cracking resulting in the leak of the working agent and/or loss of vacuum.

Further, for the best cooling performance, the plunger-driven displacer has to be axially centered and driven close to resonance. These objectives are usually achieved by providing a mechanical spring typically located in a rear chamber and supporting the warm side of a displacer from the stationary base of the cold finger, whereupon the spring rate should be chosen with respect to the mass of the displacer and desirable driving frequency. It is worth noting that such mechanical springs are prone to fatigue-caused failures. Their anchoring to the moveable displacer and static housing adds mechanical complexity, void volume, and bulk to the warm side of the cold head. Also, such springs exert essential side forces resulting in parasitic friction, wear, generation of debris and extra power draw.

Based on a unique uniformity and repeatability of the regenerator material, CryoTech adopted the concept of plungerless expander, where the pressure-drop through the regenerator drives the displacer instead of a separate plunger, as explained in [1-3]. In this method, the displacer driving force is proportional to the gas velocity through the regenerator instead of to the pressure fluctuation above and below the mean pressure.

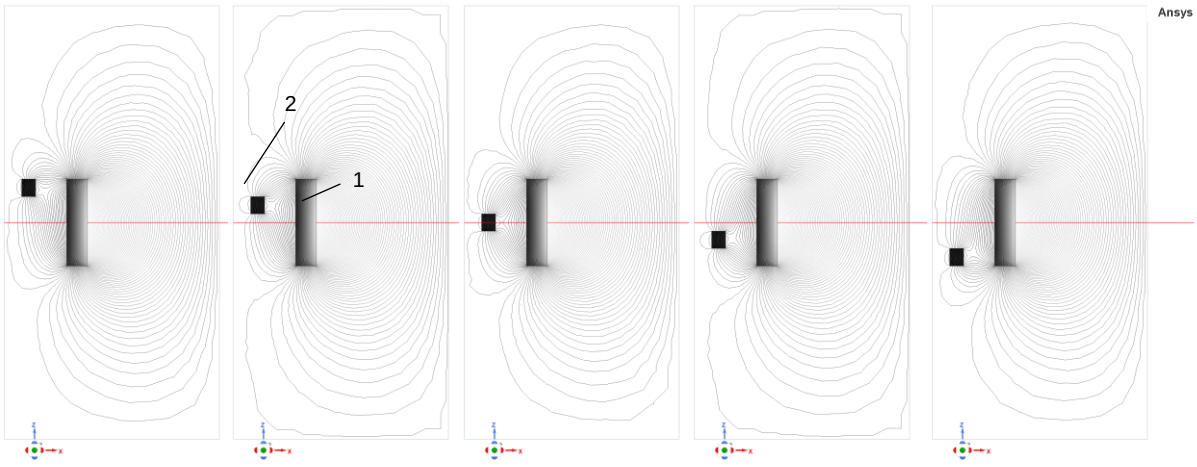

Figure 11. Magnetostatic simulation of magnet spring

There is some loss of performance with this method because, without the plunger, there is one fewer degree of freedom available for adjusting the phase angle between displacer motion and pressure fluctuation. As a result, this phase angle tends to be somewhat lower than when using a plunger. Nevertheless, this loss of this performance is amply compensated for by lower parasitic friction, pressure drops in conduits and typically complex gas passages, reduced moving mass, better exposure of the warm chamber for heat sinking, etc.

Even so, the successful full-scale testing of this design concept in a combination with magnet spring was performed on CryoTech split Stirling cryogenic cooler. Different topologies of suitable magnet springs are disclosed in CryoTech's patent application [14]. In particular, the authors managed to design a linear magnet spring comprised of the two coaxial magnet rings featuring axial and opposite directions of magnetization, where the static outer magnet ring (1) is mounted fixedly upon the cold finger base and the movable inner magnet ring (2) is fixed upon the warm side of the displacer tube, see Figure 11. Figure 11 portrays superimposed lines of magnetic flux at different axial positions of the movable magnet ring according to magnetostatic FEA software ANSYS MAXWELL.

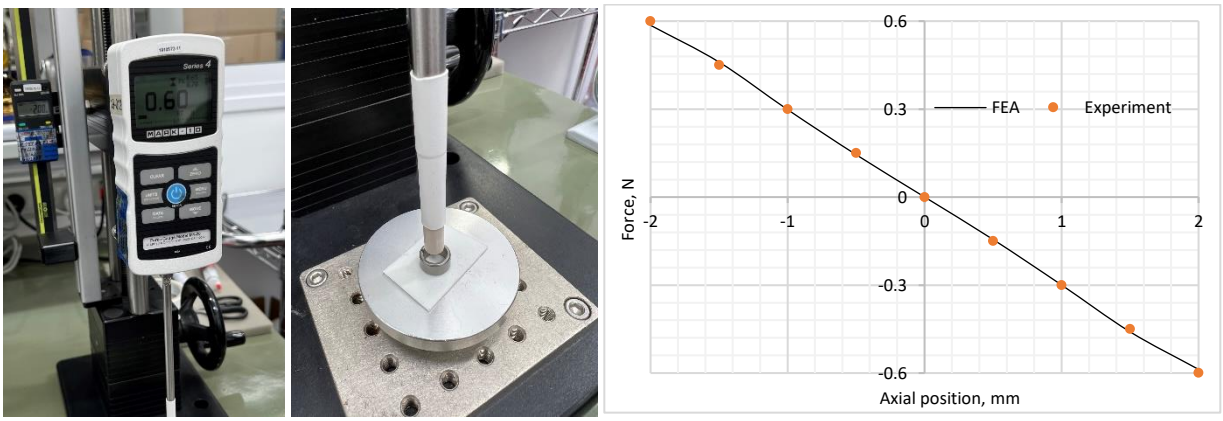

(a) (b)

Figure 12. Experimental evaluation of magnet spring

Figure 12.a shows the experimental setup and Figure 12.b compares experimental and theoretical values of the force exerted upon the movable magnet ring at different axial positions. From Figure 12, the resulting magnet spring is linear with spring rate $300\ N/m$ over the working range $\pm 2\ mm$, thus providing a resonant frequency of 105Hz for the spring assisted displacer.

Figure 13 shows the cutaway view of such an expander relying on the pneumatic plungerless displacer assisted by the magnet spring, as explained above. In Figure 13, the cold finger is constructed of the customizable SST cold finger base 1 and seamless cold finger tube 2 which is extruded of the Haynes 25 (L605) alloy and. The cold finger tube 2 is capped by the cold finger plug 3 made of Invar. All the three parts are connected by laser welding. The displacer assembly is comprised of the PEEK displacer tube 5 confining a parallel wire regenerative heat exchanger 4 in the form of a bundle of nylon filaments (diameter 9.5um, 79% porosity). The coaxially and width-mated movable axially polarized magnet ring 7, which is affixed at the warm end of displacer tube, and stationary axially and oppositely polarized magnet ring 8, which is affixed at the rear cover 6, form the magnet spring. The rear cover is attached and sealed to the compressor

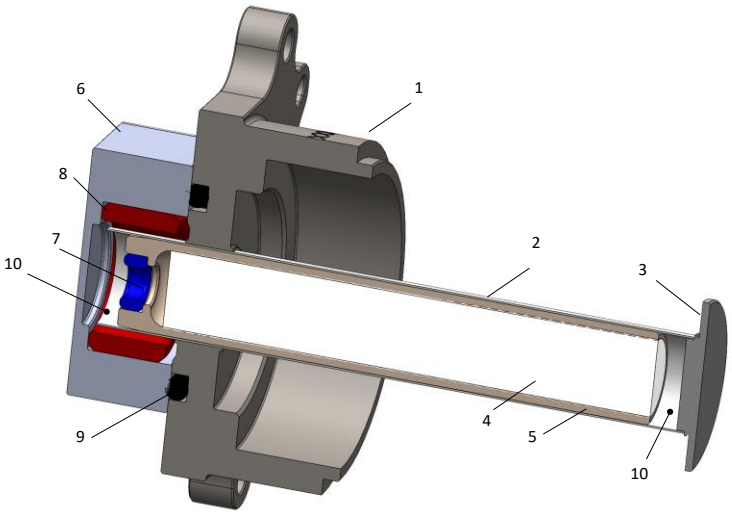

Figure 13. Cutaway view of the plungerless expander

base 1 using set of four screws (not shown) and rubber O-ring 9.

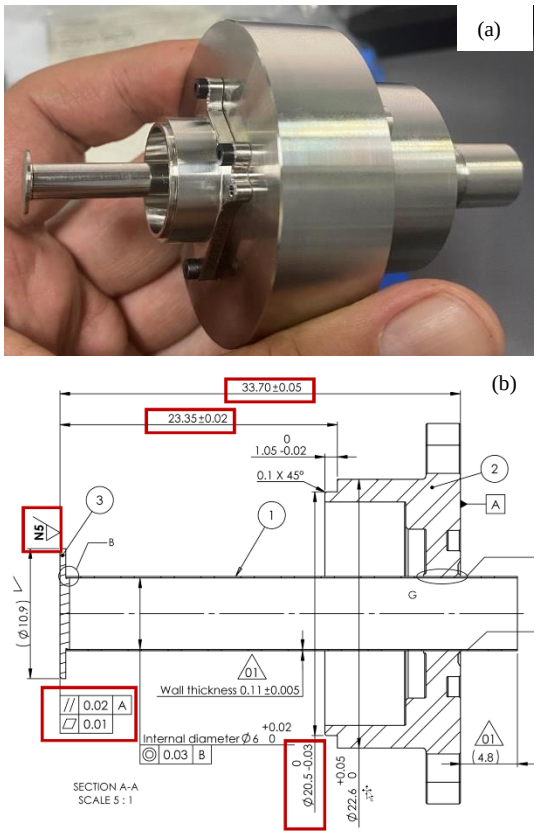

Figure 15. Post-machining of cold finger

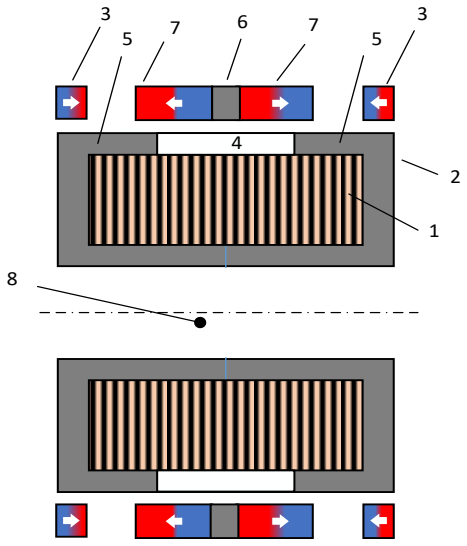

Figure 14. Inverted moving magnet actuator

The plungerless concept allows maintaining the entire displacer assembly within the cold finger tube at all times. For this purpose, the cold finger tube protrudes into the warm space of the rear cover, thus increasing the length of the clearance seals formed between tightly matched displacer and cold finger tubes (15-25 um radial gap). Such a design does not require accurate alignment of the cold finger bore and cold finger base, as typical of the plunger-driven expanders. Also, all the critical dimensions may be achieved by post-machining (turning) as shown in Figure 14.a where the mounting surface of the cold finger base is used as datum A, see Figure 14.b, where critical dimensions are marked by red: surface finish, parallelism and distance of the lobe of the cold finger plug relatively to the datum A, diameter and position of the feature for mounting Dewar shroud.

Advantages of this design concept are many. To start with, using a low weight regenerator and absence of the, usually metal, drive plunger allows substantial reduction of the weight of the moving assembly to 0.6 gr which is approximately 1/10 of the typical weight of a plunger-driven displacer with a metal stacked-screen regenerator. This results in negligibly low vibration export and lower driving force. Further, using a SST cold finger base allows for a direct connectivity to the Dewar shroud, typically made of Kovar. Further, absence of the drive plunger in combination with the compact magnet spring substantially reduces the overall length of the cold head and the bulk of the warm side.

It is also worth noting that in comparison with a cold finger machined of titanium alloy, at all other equal conditions, the resonant frequency of the cold finger made of Haynes 25 (L605) tube will be 55% higher in virtue of substantially higher module of elasticity, $E = 210\ GPa$, providing for better dynamic stability under adverse environmental conditions. Also, seamless tubes extruded of this alloy offer better ($\pm 5\mu m$ instead of $\pm 25\mu m$) tolerance on cold finger tube ID and better surface finish (N3 instead of N7). This eliminates the need for individual matching of the OD and wear of the displacer tube. Also, better ($\pm 5\mu m$ instead of $\pm 15\mu m$) tolerance on wall thickness offers better uniformity in terms of resonant frequency and axial heat conductance.

5. PISTON COMPRESSOR DRIVEN BY A MOVING MAGNET ACTUATOR

CryoTech adopted the concept of a piston compressor driven by the (patent pending) inverted moving magnet actuator [15]. Figure 15 shows the diagram of such an actuator comprised of stator and mover. The stator is comprised of the tubular driving coil 1 enveloped by the ferromagnetic toroidal back iron 2 and axially and oppositely magnetized magnet rings 3. The back iron 2 features cylindrical axial air gap 4, thus forming outward facing poles 5. The mover is comprised of the ferromagnetic tubular yoke 6 sandwiched between two axially and oppositely magnetized magnet rings 7 having polarization directions opposite to adjacent magnet rings 3, as shown by arrows in Figure 15.

In the case when there is no electric current in the driving coil and mover is placed in the mid-position, the magnets 7 are symmetrically attracted to the poles 5 and repulsed from magnets 3, thus no net force is exerted on the mover. Axial displacement of the mover from the above mid-position results in breaking the said condition of symmetry and domination of the repulsive force, thus exerting the net force directed to the initial mid-position of the mover. This results in an effect of the magnet spring producing restoring force exerted to the mover and aimed to the center of the actuator. The shape of the resulting nonlinear magnet spring may be controlled by the geometry of back iron along with moving and stationary magnet rings.

When DC electric current flows across the driving coil, depending on the current direction, one of the magnets 7 is attracted to the adjacent pole and the other is repulsed from the adjacent pole, thus producing DC net force exerted upon the mover. Application of AC current, therefore, results in AC force, the frequency and magnitude of which depends on the frequency and magnitude of AC current.

In this design concept, the central bore 8 of the actuator in Figure 15 is free of magnetic fields produced by the magnet rings and driving coil, thus allowing using ferromagnetic piston and cylinder sleeves, as explained below.

It is important to notice, the function of generating the bias magnetic flux in back iron and air gaps is split between static and moving magnet rings; this allows for reduced weight of the moving magnet rings and, therefore, the weight of the moving assembly and vibration export. This is essential for application of the single-piston compressor.

Design of the linear moving magnet actuator was performed using magnetostatic finite elements software ANSYS Maxwell. Figure 16 shows the simulated magnetic fields at different axial positions of the components of the cylinder assembly with no (a) and with 1A DC (b) in the driving coil.

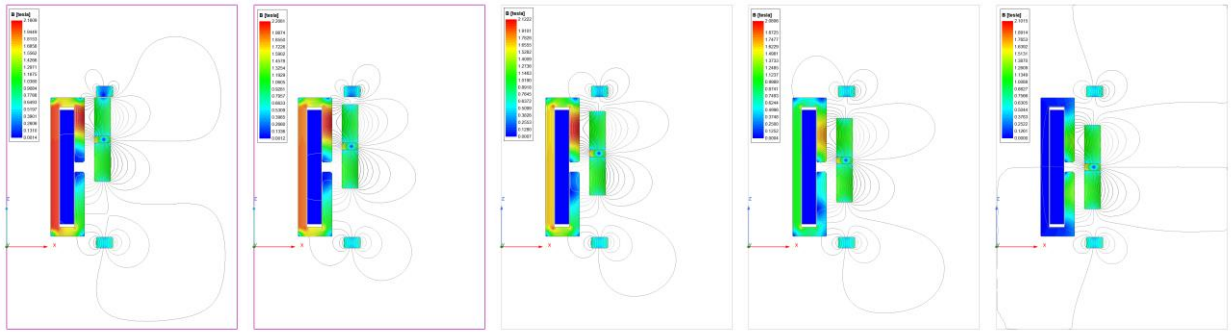

(a)

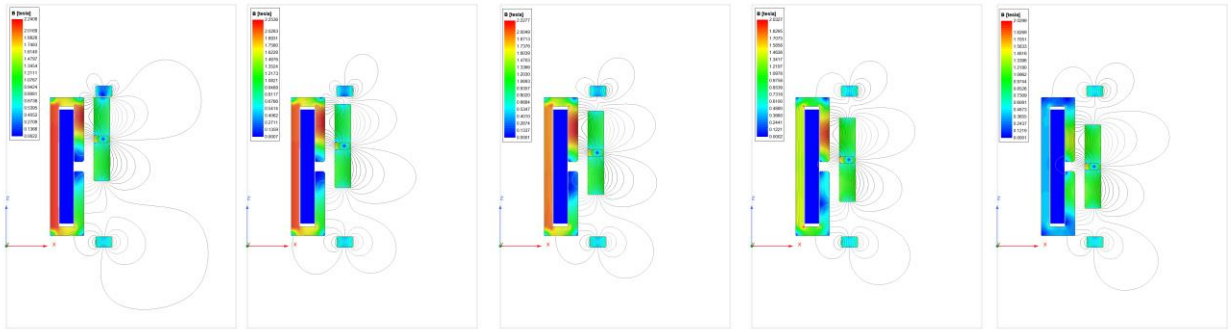

(b)

Figure 16. Simulation of inverted moving magnet actuator

Figure 17 summarizes the design of actuator. In particular, Figure 17.a shows the dependence of the force exerted upon the mover on the axial position at no current in the driving coil. Figure 17.b shows the dependence of the actuator "current to force" constant on the axial position of the mover. From Figure 17.a, within the working range typical of temperature control mode (±1mm) the resulting magnet spring is apparently linear yet within the working range typical of the cooldown mode (±2mm) the magnet spring is already slightly nonlinear. The end of stroke effects typical of the full range (±4mm) are primarily needed for the over-stroking safety.

Not less important is that such a nonlinear magnet spring appears to be very efficient tool for controlling the piston drifts resulting typically from the pressure difference build-ups following leaks of the working fluid through the piston/cylinder

clearance seals, thus eliminating the need for the pressure equalizing arrangements. From Figure 17.b, the current to force transformation curve was shaped as to have a peaky maximum in the mid position where piston velocity is maximum, as needed for the higher efficiency of the resonant actuator.

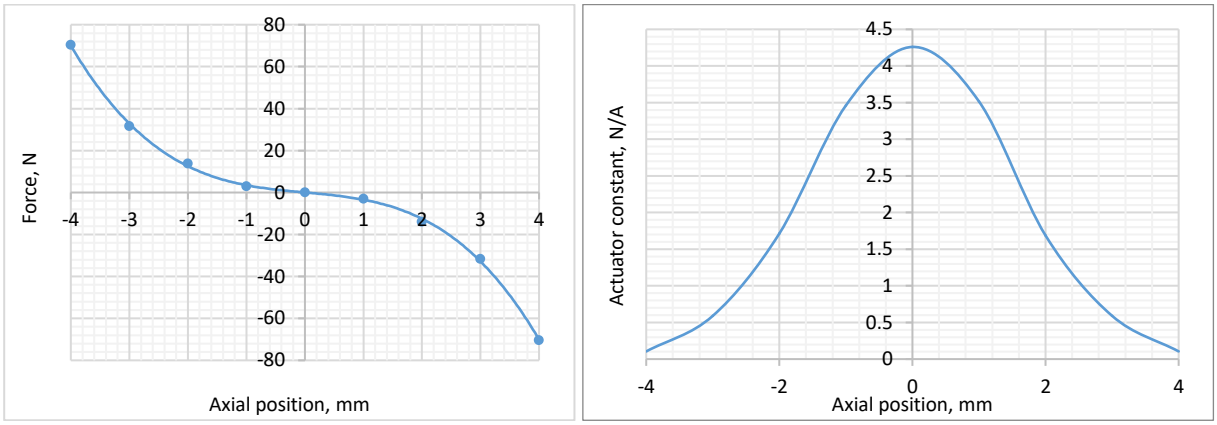

(a) (b)

Figure 17. Design of moving magnet actuator with nonlinear magnet spring

Figure 18 shows the exemplary cutaway view of single-piston compressor driven by the above explained inverted moving magnet actuator. The stator assembly is comprised of the driving coil 1 enveloped by the back iron 2 and is placed within the opened to the environment tubular pocket provided within the compressor housing 3 and encapsulated using polyurethane compound (not shown).

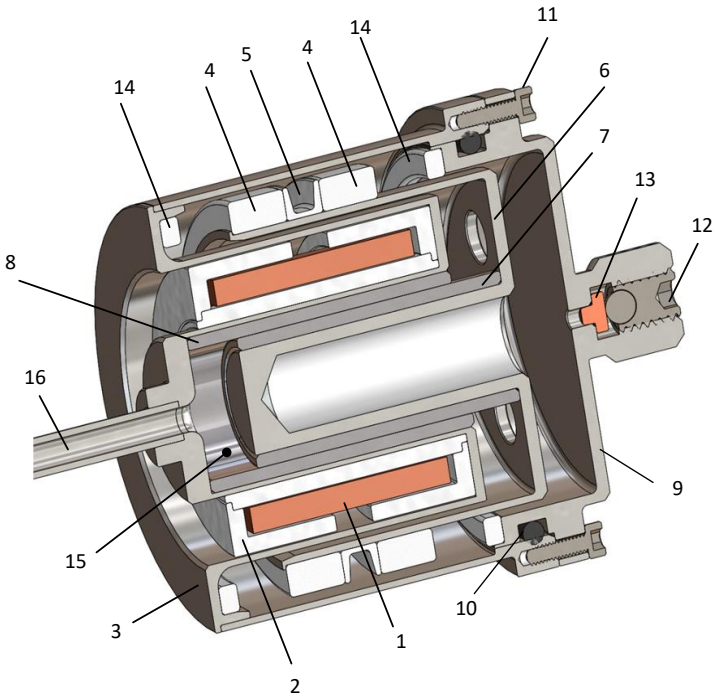

Figure 18. Cutaway view of linear compressor

The compressor mover is comprised of the magnet rings 4 and moving ferromagnetic yoke 5 which are coaxially bonded upon the magnet holder 6 featuring the hollow piston shaft being externally lined with the hard and wear resistant piston sleeve 7 made of high-speed tool steel M42. The liner was hardened to 65HRc and its OD ground to N3. The cylinder sleeve 8 is made of the same material and bonded inside the central bore of the compressor housing. The nominal radial gap between piston and cylinder sleeves is 12um, thus forming close clearance seals and guide for the axial sliding the piston assembly comprised of parts 4,5,6,7. The rear cover 9 is sealed against and attached to the compressor base using a radial O-ring seal 10 and screws 11; provision is made for the fill/purge valve comprising swivel-ball set screw 12 and copper seal 13. Two stationary magnet rings 14 are bonded to the housing and rear cover coaxially with the mover. The compression chamber 15 is in pneumatic communication with the warm chamber of the cold head using the transfer line 16.

6. MECHANICAL DESIGN OF SPLIT LINEAR CRYOCOOLER

Figure 19 shows 3D rendering and dimensional views of the side-by-side placed compressor 1 and cold head 2 interconnected by the transfer line 3 (split design).

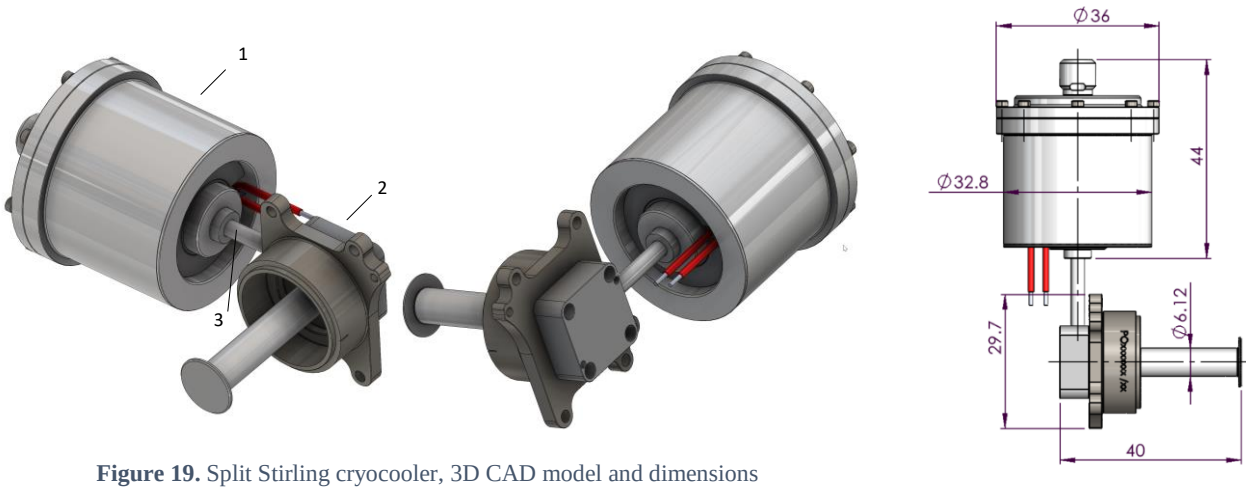

Figure 19. Split Stirling cryocooler, 3D CAD model and dimensions

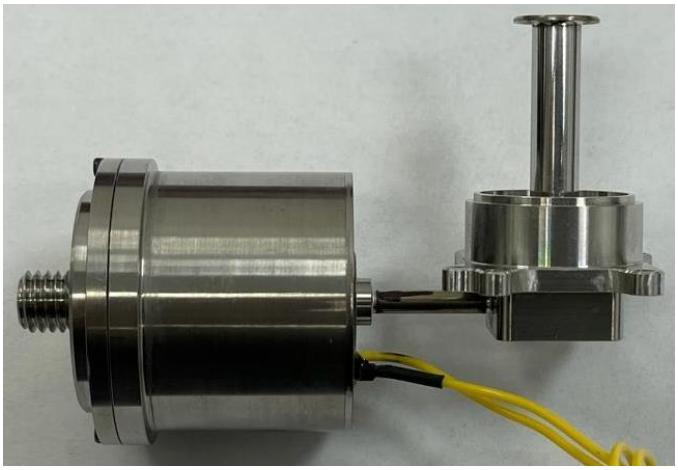

Figure 20. Assembled split Stirling cryocooler

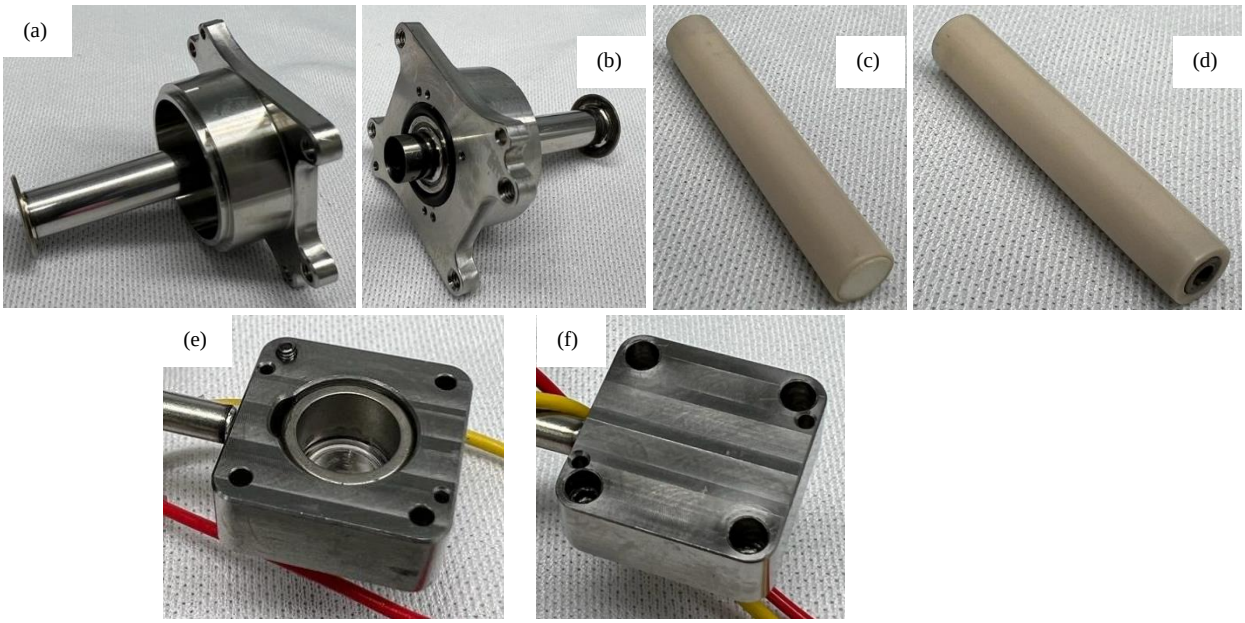

Figure 21. Expander subassemblies

Figure 20 pictures the assembled cryocooler, the total weight of which is 115 gr (cold finger excluded). Figure 21 shows components of the expander: (a,b) – cold finger, (c,d) - displacer assembly with bonded movable magnet ring and inserted regenerator, (e,f) – rear cover with bonded stationary magnet ring and welded transfer line.
Figure 22 shows components of the linear compressor: (a) – edgewise driving coil, (b) - stator assembly, (c,d) – compressor housing prior to cylinder sleeve bonding and stator encapsulation, (e,f) - compressor housing after cylinder sleeve bonding and stator encapsulation, (g,h) – piston assembly with magnet rings, moving yoke and piston sleeve , (i,j) – rear cover with fill/purge valve and static magnet ring.

Figure 22. Compressor: components and subassemblies

7. PRELIMINARY TESTING

Preliminary testing was performed using split configuration upon integration of simulation Dewar having heat load 210mW@150K@23C (courtesy of Lynred), as shown in Figure 23.
Figure 24.a shows the experimentally evaluated load curves – dependencies of the power consumption in the temperature control mode 150K on the added heat load at different reject temperatures. It is worth noting that by varying charge pressure and driving frequency the cryocooler may be further optimized for different working conditions. Figure 24.b shows dependencies of the compressor coefficient of performance (COP) and power factor (PF) on the power consumption over the typical range 0-10W. From Figure 23.b, both dependencies are flat over the entire range of power consumptions. It is worth noting that the COP of such a small compressor is relatively high even at low power consumptions. Closeness of power factor to unity indicates closeness to resonance and simplifies design of electronic driver.

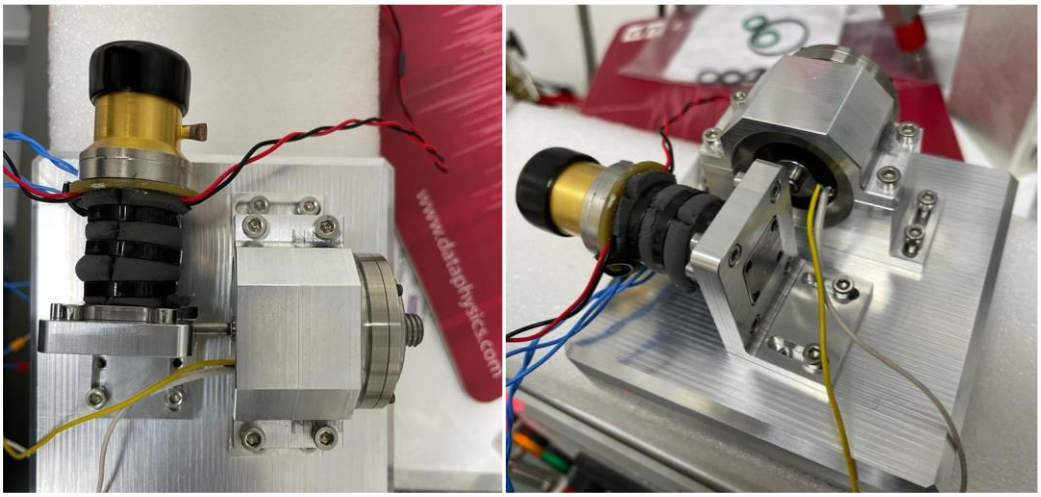

Figure 23. Split cryocooler under test

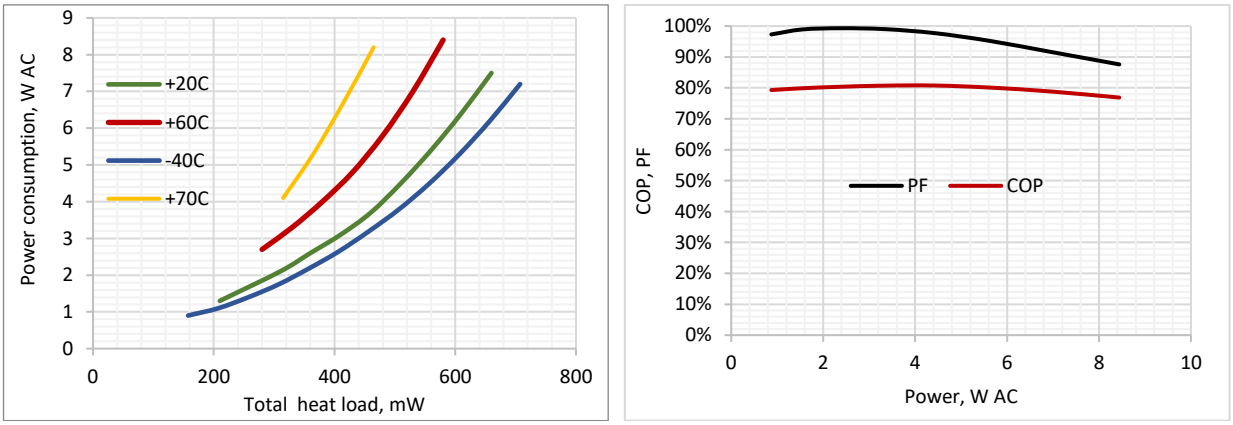

(a) (b)

Figure 24. Load curves and compressor evaluation

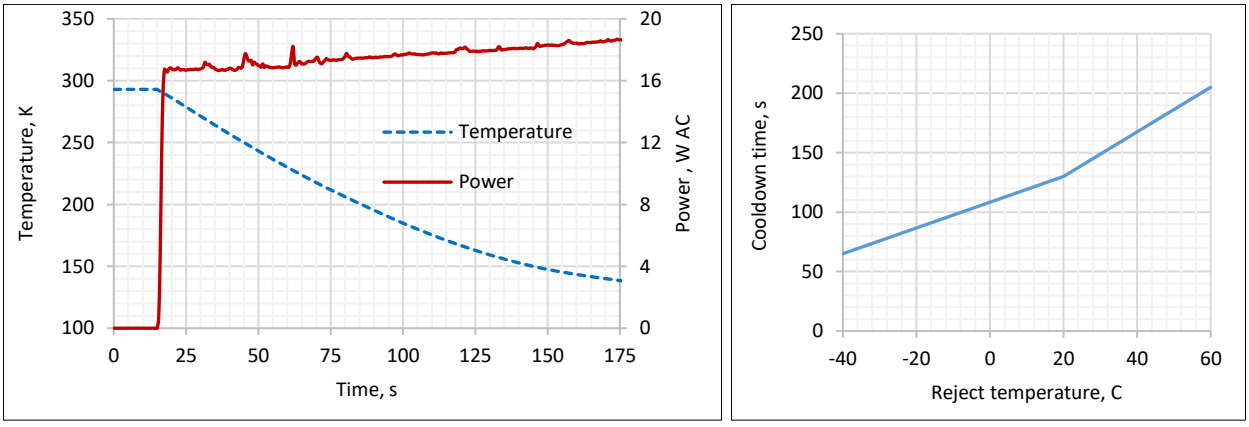

(a) (b)

Figure 25. Cooldown at +20C (a) and cooldown times at different reject temperatures (b).

Figure 25.a shows the time history of the temperature and power draw during “open loop” cooldown phase at the reject temperature of +20C; the maximum power consumption was trimmed to be below 18 W AC. From Figure 25.a, the cooldown time is 130s. Figure 25.b shows the dependence of the cooldown time on the reject temperature.

ACKNOWLEDGMENTS

The authors are thankful to Israel Innovation Authority for providing generous financial support for this project.

CONCLUSIONS

The objective of ultimate reduction of manufacturing costs while keeping high reliability and performance indices has been achieved by making use of

- alternative leak-free working fluid, the real gas properties of which enable for additional Joule-Thomson cooling effects over the range of working temperatures typical of HOT IR detectors
- commercially-off-the-shelf available nylon “parallel wire” microfiber material for regenerative heat exchanger having high uniformity, exceptionally low axial heat conductivity, friction factor and thermal mass while providing for sufficient thermal penetration depth and optimum hydraulic diameter.
- plungerless pneumatic actuation of displacer assembly relying on the drag force produced by the regenerator material, thus allowing for elimination of the expensive and bulky differential pneumatic actuator
- failure-free linear magnet springs, thus replacing mechanical springs in both compressor and expander
- inverted moving magnet actuator with axially magnetized moving and static magnet rings along with low cost edge-wise driving coil having exceptionally high copper fill factor (>90%), thus allowing for essential reduction the weight of moving assembly without affecting electromechanical COP
- single piston compressor with lightweight moving assembly and low vibration export
- optional tuned dynamic absorber for vibration sensitive applications
- simplified cold finger made of seamless tube extruded of L605 alloy welded to the SST cold finger base requiring no accurate alignment of the cold finger tube and cold finger base and simplifying connection to the Dewar shroud

CryoTech presented the theoretical substantiation and full-scale feasibility study of novel cryogenic technologies paving way to a new generation of low SWAP+C cryogenic coolers for HOT IR imaging.

REFERENCES

[1] Veprik, A., Tavori, A., Raviv Z., Zehctser S., Refaeli R., Wise, A. “Low cost cryogenic coolers for commercial infrared imagers”, 11002, Infrared Technology and Applications XLV, 1100203 (2019)
[2] Veprik, A., Zechtser, S., Refaeli, R., and Wise, A. "Affordable cryocoolers for commercial IR imaging," Proc. SPIE 11741, Infrared Technology and Applications XLVII, 117410G (2021)
[3] Veprik, A., Kurucz, S. and Refaeli, R., “Low-cost cryogenic technology for commercial infrared imaging”, Cryocoolers 22, 127-135 (2022)
[4] Schwertz, F. A., “Diffusivity of water vapor in some common gases”, Journal of Chemical Physics, V 19 (5), 640–646 (1951)
[5] Ross, R., G., Jr. “Cryocooler reliability and redundancy considerations for long-life space missions”, Cryocoolers 11, 637-648 (2000)
[6] Gedeon, D., Sage pulse tube model-class reference guide, Gedeon Associates (2021)
[7] https://www.nist.gov/srd/refprop
[8] Snodgrass, R., Kotsubo, V., Ullom, J. and Backhaus, S., “Leveraging real fluid effects as a tool for power flow measurements in 4 K cryocooler regenerators”, Cryocoolers 21, 315-324 (2021)
[9] Nam, K. and Jeong S., “Development of parallel wire regenerator for cryocoolers”, Cryogenics, V46, 4, 278-287 (2006)
[10] Lewis, M. A., Kuriyama, T., Kuriyama F. and Radebaugh R., “Measurement of heat conduction through stacked screens”, Advances in Cryogenic Engineering, V 43, 1611-1618 (1998)

[11] Lewis, M.A. and Radebaugh, R., “Measurement of heat conduction through bonded regenerator matrix materials”, Cryocoolers 12, 517-522 (2003)
[12] https://trc.nist.gov/cryogenics/materials/materialproperties.htm
[13] Kays, W.M and London, A.L., Compact heat exchangers, 3rd edn., McGraw Hill (1984)
[14] Veprik, A., “Expander unit with magnetic spring for a split Stirling cryogenic refrigeration device”, US 2022/0250169 A1, EP4092354A2, CN115371282A (2023)
[15] Veprik, A., “Compressor unit of a split Stirling cryogenic refrigeration device”, US 2023/00174114 A1, EP 4 119 865 A1, CN115614248A (2023)